Reversible Control of Magnetic Anisotropy and Magnetization in Amorphous $Co_{40}Fe_{40}B_{20}$ Thin Films via All-Solid-State Li-ion Redox Capacitor

Dhanapal Pravarthana,[1,2] Baomin Wang,[1,2,*] Zeeshan Mustafa,[1,2] Sandeep Agarwal,[1,2,3] Ke Pei,[1,2] Huali Yang,[1,2] and Run-Wei Li[1,2,4,†]

[1] *CAS Key Laboratory of Magnetic Materials and Devices, Ningbo Institute of Materials Technology and Engineering, Chinese Academy of Sciences, Ningbo 315201, People's Republic of China*

[2] *Zhejiang Province Key Laboratory of Magnetic Materials and Application Technology, Ningbo Institute of Materials Technology and Engineering, Chinese Academy of Sciences, Ningbo 315201, People's Republic of China*

[3] *Department of Physics, Government Engineering College, Bhojpur, Old IIT Campus, Patliputra, Patna 800013, India*

[4] *Center of Materials Science and Optoelectronics Engineering, University of Chinese Academy of Sciences, Beijing 100049, People's Republic of China*

(Received 29 April 2019; revised manuscript received 9 October 2019; published 27 November 2019)

The emerging field of ionics-controlled magnetism is highly promising towards switching magnetism on and off magnetism at the touch of a button and efficient low-power-consumption spintronic devices. It can be achieved through the doping of ions, such as O^{2-} and Li^{+}, into reactive magnetic materials. The advantages of a solid-state electrolyte far exceed those of a conventional electrolyte. Here, we utilize the all-solid-state Li^{+} redox capacitor structure to modulate the magnetism of amorphous $Co_{40}Fe_{40}B_{20}$ thin films. The change in magnetism of $Co_{40}Fe_{40}B_{20}$ due to lithiation-delithiation is investigated by measuring its magnetic hysteresis loop along the out-of-plane (in-plane) direction under the charge (discharge) state. Reversible saturation magnetization of 27% in $Co_{40}Fe_{40}B_{20}$ thin films is achieved due to conversion reactions with Li^{+}. Further lithiation causes the out-of-plane axis to become harder, and thus, leads to an increase in the magnetic anisotropy along the in-plane direction. This provides a means to control the magnetic properties of metallic magnetic thin films by solid-state ionics.

DOI: 10.1103/PhysRevApplied.12.054065

I. INTRODUCTION

Ionics modulation of a functional material has a huge potential to offer tunable, or on and off switching of its functional properties, and the induction of novel functionalities in a reversible way [1–3]. This approach enables *in situ* control, low power consumption, freedom from structural disorder, and high integration with the technology platform [4]. Indeed, functional properties, such as superconductivity, catalysis, magnetism, magnetoresistance, photoluminescence, and synaptic plasticity, can be controlled by ionics [1,4,5]. In particular, it is highly promising to control magnetism by ionics to achieve efficient and low-power-consumption spintronic devices [6]. The modulation of magnetism can be achieved in two ways based on whether the ionic source is generated within the magnetic structure or from the external ionic source. Magnetic modulation, in the case of an ionic source located within the magnetic structure, is limited to the nanoscale [7]. Alternatively, in the case of an external ionic source, magnetic modulation can be achieved from the nanoscale to macroscale. Various magnetoionic devices can be engineered for magnetic modulation, such as the electric double-layer structure, the electric double-layer transistor structure, a hybrid supercapacitor, and a Li-ion battery [8–17]. The electric double-layer structure is limited to interfaces due to electrostatic carrier doping [5,18]. In the other three approaches, electrochemical carrier doping takes place via redox reactions. This doping can penetrate into the bulk of a material to control magnetism beyond the interface. Redox reactions can take place by electrochemical doping of ions such as H^{+}, O^{2-}, Li^{+}, and Si^{+} [2,3,19].

Previously, O^{2-} doping has been explored for the control of perpendicular magnetic anisotropy in Co and $Co_{60}Fe_{20}B_{20}$ ultrathin films [20–22], but high voltage, high working temperature, and prolonged voltage application time are some of the drawbacks of utilizing O^{2-} as a doping ion, to enable its diffusion into the magnetic host

*wangbaomin@nimte.ac.cn
†runweili@nimte.ac.cn

material to undergo reversible chemical reactions. Alternatively, Li^+ ions promise more advantages, as they can diffuse rapidly at high concentrations at room temperature because they are lightweight and smaller radii in comparison with O^{2-}. In addition, the chemistry of lithiation has been extensively explored in the field of Li^+ batteries for materials of various compositions and structures for the development of cathode and -anode materials [23–27]. The lithiation process into electrode materials can be broadly classified into three categories, namely, insertion, alloying, and conversion reactions [26]. This enables a larger platform to design a magnetoionic device based on Li^+ reactions as the doping element. For example, magnetic oxides, such as Fe_2O_3 and Fe_3O_4, can undergo a conversion reaction with Li^+, as O^{2-} is electronegative element, leading to the formation of Li_2O and Fe metal under lithiation that leads to reversible magnetic cycling and modulation of magnetization [12,16]. However, magnetic metal electrodes have not been explored for lithiation in the context of magnetic modulation. Here, we explore the magnetic modulation of amorphous $Co_{40}Fe_{40}B_{20}$ magnetic metal electrode by lithiation, as it can undergo a lithiation conversion process with electronegative B element to allow alloying reactions. We perform detailed characterizations of the modulation of magnetism in $Co_{40}Fe_{40}B_{20}$ by lithiation-delithiation. Reversible saturation magnetization of 27% in $Co_{40}Fe_{40}B_{20}$ thin films is achieved by conversion reactions with Li^+. Also, under lithiation, the out-of-plane axis becomes harder, leading to an increase in magnetic anisotropy along the in-plane direction. This study opens the way to explore magnetic alloys and the control of magnetism by Li^+ ionics for storage devices. Thus, the properties of a magnetic device can be controlled by solid-state ionics.

II. EXPERIMENTAL

A. Sample preparation

Solid electrolyte lithium-ion conductor glass ceramic (LICGC) AG-01 plates with dimensions of 25×25 mm^2 and a thickness 0.15 mm are purchased from OHARA INC, Japan. One side of the plate is polished using diamond polishing liquids to low roughness. We then deposit $LiCoO_2$ (LCO) of 250 nm thick by pulsed laser deposition (PLD) at a deposition temperature of 600 °C under 10 Pa oxygen pressure using a KrF excimer laser ($\lambda = 248$ nm) with a repetition rate of 2 Hz. Then, Pt film of 150 nm thick is deposited over LCO for electrical connection by magnetron sputtering. The other surface of the LICGC is polished to low roughness using diamond polishing liquids. This polished side is used to deposit $Co_{40}Fe_{40}B_{20}$ of 200 nm thick by magnetron sputtering under 1.2 Pa argon pressure and 100 W. Then, a Pt film of 15–150 nm thick is deposited over $Co_{40}Fe_{40}B_{20}$ for electrical connection.

B. Structural and magnetic characterization

The phase and purity of the $Co_{40}Fe_{40}B_{20}$ and LCO films are characterized by x-ray diffraction on a D8 Bruker ADVANCE DAVINCI diffractometer using a Cu $K\alpha$ ($\lambda = 1.5406$ Å) source. The samples for transmission electron microscopy (TEM) studies are prepared by focused ion beam using a Carl Zeiss double-beam scanning electron microscope. A transmission electron microscope (JEM-2100F TE) operating at 200 kV is utilized to investigate the structure of the films. The chemical composition and bonding states are measured by XPS using a Kratos AXIS ULTRA^{DLD} instrument with a monochromic Al $K\alpha$ x-ray source ($h\nu = 1486.6$ eV). A superconducting quantum interference device (SQUID) is utilized to measure the magnetic hysteresis loop of $Co_{40}Fe_{40}B_{20}$ films. Atomic force microscopy (AFM), on a Bruker, Dimension ICON microscope, integrated with conductive atomic force microscopy (cAFM) and magnetic force microscopy (MFM) is utilized to characterized the current flow and magnetic domain.

C. Electrochemical characterization

A Zahner Zennium electrochemical workstation is utilized to measure cyclic voltammetry (CV), galvanostatic charge-discharge cycles, and electrochemical impedance spectroscopy (EIS) in the all-solid-state Li^+ redox capacitor structure. In all electrochemical measurements, the $Co_{40}Fe_{40}B_{20}$ anode film is used as working electrode, with LCO as counter and reference electrodes. The CV measurements are performed between -1 and 3 V versus Li/Li^+ at a scanning rate of 100 mV/s. The galvanostatic charge-discharge cycles are performed at constant current, ranging from 0.3 to 2 μA. The EIS measurements are performed over the frequency range between 10^{-1} and 10^5 Hz under a current of 1 mA.

III. RESULTS AND DISCUSSION

A. All-solid-state magnetoionic redox capacitor structure

We use an all-solid-state Li^+ redox capacitor structure, consisting of LICGC as a solid electrolyte, to modulate the magnetism of amorphous $Co_{40}Fe_{40}B_{20}$ thin films, as described in Fig. 1(a). In this structure, $Co_{40}Fe_{40}B_{20}$ acts as the anode material and LCO acts as the cathode material, which supplies Li^+ to $Co_{40}Fe_{40}B_{20}$ to modulate its magnetism. The Pt electrode is chosen as top and bottom electrodes as it is stable under a high-voltage bias [28]. The polished LICGC substrate, with an average roughness is 0.2 nm, is used to deposit LCO by PLD with an average roughness of 5.5 nm, as shown in Fig. 1(b). The other side of LICGC is polished to deposit $Co_{40}Fe_{40}B_{20}$, with an average roughness of 2 nm, as shown in Fig. 1(c). The structure and purity of the LCO and $Co_{40}Fe_{40}B_{20}$ film is

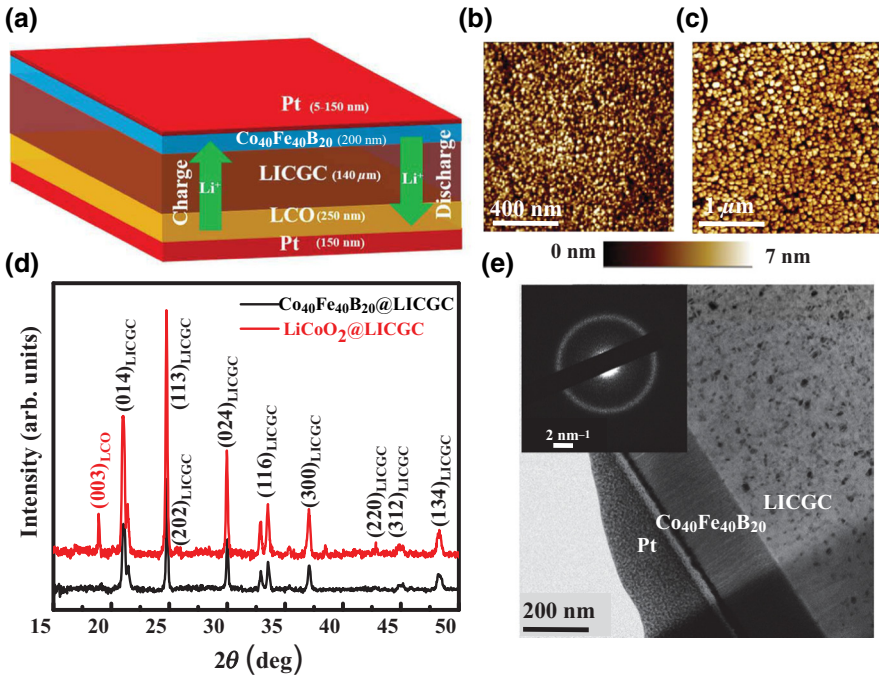

FIG. 1. (a) Schematic of all-solid-state Li^+ redox capacitor comprising of LICGC as solid electrolyte with LCO and $Co_{40}Fe_{40}B_{20}$ as cathode and anode materials, respectively. The Pt electrode is utilized as both positive and negative current collectors. A thick (150 nm) and thin (15 nm) Pt electrode over $Co_{40}Fe_{40}B_{20}$ anode material is used as electrical contact for macroscale and nanoscale modulations, respectively. Typical topography images obtained by tapping-mode AFM of (b) LCO and (c) $Co_{40}Fe_{40}B_{20}$ surfaces. (d) An XRD pattern of LCO (150 nm) and $Co_{40}Fe_{40}B_{20}$ (200 nm) films. (e) Cross-section low-magnification bright-field transmission electron micrograph of $Co_{40}Fe_{40}B_{20}$/LICGC interface; a selected-area electron diffraction pattern is inset in the top-left corner.

investigated by XRD, as shown in Fig. 1(d). The Braggs diffraction peaks of the LICGC substrate are well indexed, and the (003) peak, corresponding to the LCO rhombohedral crystal system, with the *R*-3*m* space group, is observed [29]. The peak corresponding to $Co_{40}Fe_{40}B_{20}$ is absent, which indicates that it is amorphous in nature. Further, the amorphous nature is confirmed from the selected-area diffraction pattern obtained by cross-section TEM, as shown in Fig. 1(e), in which no diffractions spots are observed over the region of $Co_{40}Fe_{40}B_{20}$.

B. Lithium ionics into $Co_{40}Fe_{40}B_{20}$ films

Lithium ionics into the $Co_{40}Fe_{40}B_{20}$ thin film is investigated to understand the Li^+ diffusion process qualitatively and quantitatively. The all-solid-state structure of Pt/LCO/LICGC/$Co_{40}Fe_{40}B_{20}$/Pt can be viewed as a battery structure with LCO and $Co_{40}Fe_{40}B_{20}$ as the cathode and anode, respectively. Indeed, the battery structure generates an open-circuit voltage (OCV) of 0.5 V, which arises due to Li^+ storage in the LCO active material due to the difference in electrochemical potentials between the cathode (LCO) and anode ($Co_{40}Fe_{40}B_{20}$), with respect to LICGC electrolyte [26]. The lower OCV observed is a limiting factor for practical battery applications, but, for magnetic modulation, Li^+ in LCO can be utilized to charge or discharge $Co_{40}Fe_{40}B_{20}$ in capacitor mode. To understand the electrochemical redox process and to determine the charge and discharge potential, CV is carried out by cycling a $Co_{40}Fe_{40}B_{20}$ working electrode between −1 and 3 V at a scan rate of 100 mV/s. Figure 2(a) shows the CV response for the 1st, 5th, 10th, and 20th cycles, with oxidation and reduction current peaks due to lithiation and delithiation processes, respectively. The voltage of the oxidation and reduction peak currents occur at 0 and 1.5 V, respectively. This indicates stable and reversible conversion reactions between $Co_{40}Fe_{40}B_{20}$ and lithium. Then, $Co_{40}Fe_{40}B_{20}$ is used as a capacitor working electrode for galvanostatic charge and discharge voltages of 2 and −0.8 V, respectively, for 1000 cycles. The first and last five cycles of galvanostatic charge-discharge are shown in Fig. 2(b). These charge and discharge voltages are chosen to complete the charge and discharge processes, in accordance with the CV measurements [14]. The specific charge-discharge capacity, *C*, value of the $Co_{40}Fe_{40}B_{20}$ film can be determined (Eq. 1) from the galvanostatic charge-discharge curve by

$$C = \frac{I\Delta t}{m\Delta V}, \tag{1}$$

where *I* is the constant charge-discharge current, Δt is the charge-discharge time, *m* is the mass of the $Co_{40}Fe_{40}B_{20}$ thin film, and ΔV is the potential window [30]. The capacity of charge-discharge cycling for the 1st, 100th, 500th, and 1000th cycles between 2 and −0.8 V is shown in Fig. 2(c). The typical charge-discharge profile exhibits a nonlinear nature that indicates redox reactions between Li^+ and the $Co_{40}Fe_{40}B_{20}$ anode [30]. The capacitance arises from redox reactions rather than electrical double-layer capacitance because in the latter a triangular charge-discharge profile would be observed. The first 100 cycles show a reversible capacity of 34 mA h g^{-1}, but the 500th cycle shows a reversible capacity of 27 mA h g^{-1}, which is 79% of the initial reversible capacity; this decrease in capacity can be attributed to irreversible

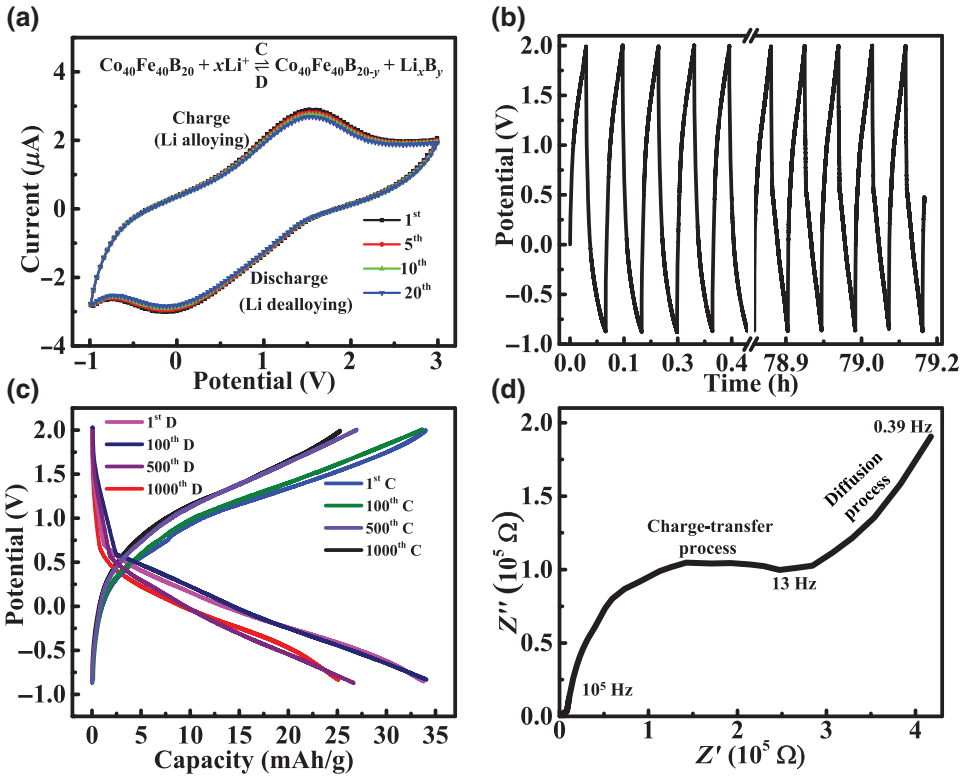

FIG. 2. (a) Cyclic voltammograms from −3 to 3 V versus Li/Li^+ at a scan rate of 100 mV/s for different cycles. The inset shows the chemical equation describing lithiation and delithiation into $Co_{40}Fe_{40}B_{20}$ under charge (C) and discharge (D), respectively. (b) First (1–5th) and last (996–1000th) five galvanostatic charge-discharge curves of the capacitor cycled at a constant current value of 0.3 μA. (c) The charge-discharge capacity for the 1st, 100th, 500th, and 1000th cycles. (d) A typical Nyquist plot of $Pt/Co_{40}Fe_{40}B_{20}/LICGC/LiCoO_2/Pt$ at a charged voltage of 2.5 V over the frequency range from 0.39 to 10^5 Hz.

capacity loss. The irreversible capacity loss is mainly attributed to volume change and local structural alterations [24]. This irreversible capacity loss can be attributed to the formation of inactive lithium boron alloy that does not undergo conversion reactions. After the 500th cycle, the reversible capacity is stable up to the 1000th cycle, with a decrease of 4 mA h g^{-1} in the reversible capacity. Amorphous $Co_{40}Fe_{40}B_{20}$ provides an elastic matrix to accommodate strain due to the volume expansion after lithiation in the 100th cycle, as Co and Fe are ductile in nature, and improve the electrical conductivity that results in reversible capacity after the 100th cycle [26]. However, the reversible capacity value is much lower than that of the theoretical storage capacity in boron. Elemental boron has higher theoretical lithium storage capacities, depending on lithium boron alloy formation, such as 2846, 3046, 4873, and 7309 mA h g^{-1} for forming the Li_7B_6, Li_5B_4, Li_2B, and Li_3B phases, respectively [31]. Further, to confirm the capacitive behavior, EIS measurements are performed to compute the Nyquist plot, as shown in Fig. 2(d). The two distinct features of impedance nature can be observed in two frequency regimes. In the low-frequency regime, the impedance is linear due to Li^+ diffusion, as a result of capacitive behavior [32]. The hemisphere in the high-frequency regime appears because of charge-transfer resistance due to interfacial resistance between LICGC and $Co_{40}Fe_{40}B_{20}$. The hemisphere can arise from resistance due Li^+ diffusion inside the $Co_{40}Fe_{40}B_{20}$ electrode [33].

C. Visualization of lithium ionics into $Co_{40}Fe_{40}B_{20}$ films

To further understand the lithiation and delithiation process into the $Co_{40}Fe_{40}B_{20}$ film, cAFM measurements are performed. The TUNA current image under a sample bias voltage of 2 V to LCO is shown in Fig. 3(a). The positive potential of LCO forces Li^+ into the top $Co_{40}Fe_{40}B_{20}$ layer. This results in an upward current flow that is visible as light-green contrast in the TUNA current image. The light-green contrasts are not homogeneous and there are gaps in between that indicate the Li^+ diffusion path. At 0 V, the current flows downward due to the discharge of Li^+ stored in $Co_{40}Fe_{40}B_{20}$ [Fig. 3(b)]. A further negative bias of −2 V leads to a downward current flow, as shown in Fig. 3(c). The black contrast represents the downward current flow due to delithiation from the $Co_{40}Fe_{40}B_{20}$ film.

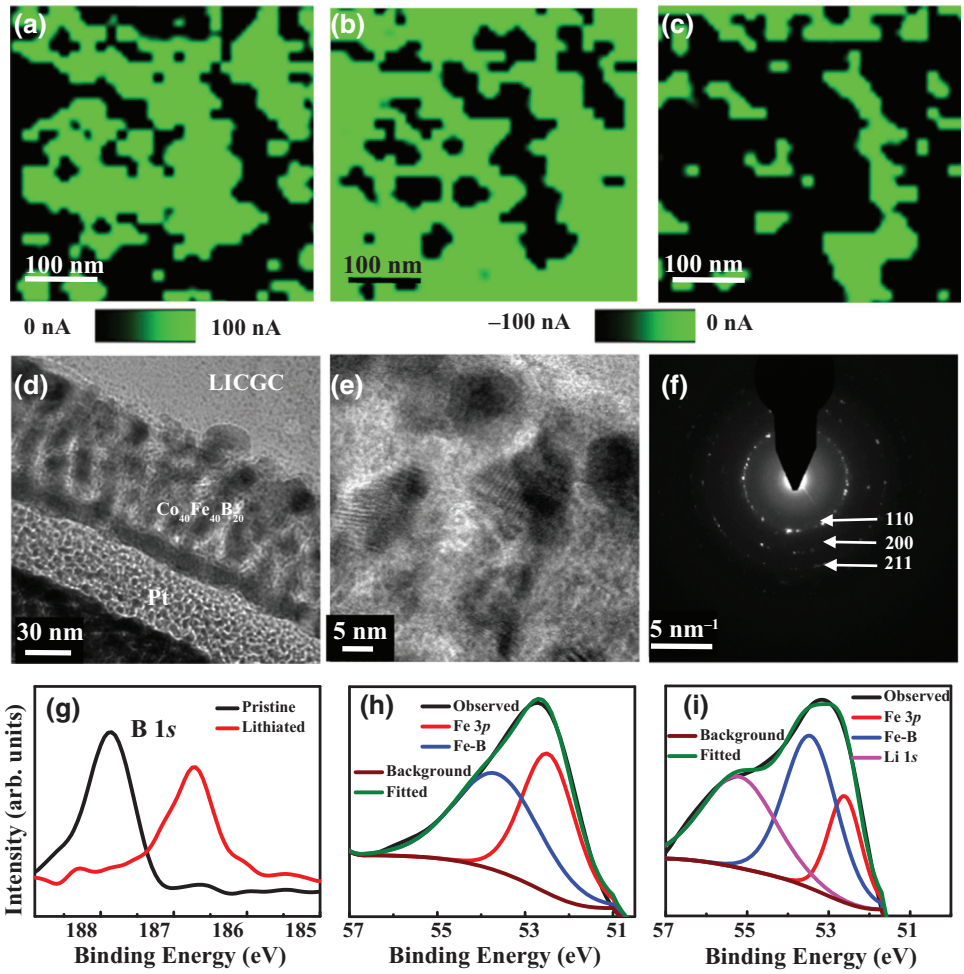

FIG. 3. TUNA current image of the lithiation-delithiation process into the $Co_{40}Fe_{40}B_{20}$ film under bias voltages of (a) 2 V, (b) 0 V, and (c) −2 V. (d) High-magnification bright-field cross-section transmission electron micrograph of the $Co_{40}Fe_{40}B_{20}$/LICGC interface after lithiation. (e) High-resolution transmission electron micrograph over $Co_{40}Fe_{40}B_{20}$ film region. (f) Selected-area electron diffraction pattern corresponding to the region over the $Co_{40}Fe_{40}B_{20}$ film. High-resolution x-ray photoelectron spectra of (g) B 1*s* lithiated-unlithiated $Co_{40}Fe_{40}B_{20}$ films and Fe 3*p* core-level spectra in (h) unlithiated and (i) lithiated states.

Moreover, the same lithiation region (green contrast) in Fig. 3(a) appears in black contrast in the delithiation region in Fig. 3(c), which shows the same diffusion for delithiation and confirms reversible lithiation-delithiation from the $Co_{40}Fe_{40}B_{20}$ film. However, the difference in some regions can be attributed to discharge of Li^+ at 0 V, which also indicates the nonvolatile nature of Li^+ storage in $Co_{40}Fe_{40}B_{20}$. To better understand the lithiation process, the cross-section sample of lithiated $Co_{40}Fe_{40}B_{20}$ film is probed by TEM, as shown in Figs. 3(d)–3(f). The $Co_{40}Fe_{40}B_{20}$/LICGC interface is intact after lithiation, as shown in Fig. 3(d). However, some fraction of Co-Fe nanocrystals can be observed in the $Co_{40}Fe_{40}B_{20}$ amorphous matrix in the high-resolution transmission electron micrograph in Fig. 3(e). The selected-area electron diffraction pattern, as shown in Fig. 3(f) over the $Co_{40}Fe_{40}B_{20}$ film region, exhibits a ring pattern that corresponds to polycrystalline Co-Fe nanocrystals, and the (*hkl*) planes index well with the Co-Fe crystal. The formation of Co-Fe crystals can be attributed to the result of the conversion reaction between lithium and $Co_{40}Fe_{40}B_{20}$. Further, high-resolution x-ray photoelectron spectroscopy (HRXPS) for lithiated and pristine $Co_{40}Fe_{40}B_{20}$ films is carried out to understand the chemical bonding of Li^+. In Fig. 3(g), the B 1*s* core-level spectrum peak corresponding to elemental boron can be observed at 188.7 eV [34]. Upon lithiation, the B 1*s* peak decreases to 186.7 eV due to the formation of the lithium–boron bond [31]. The metallic nature of the Fe 3*p* core-level spectrum peak in $Co_{40}Fe_{40}B_{20}$ is observed at 52.4 eV, as shown in Fig. 3(h). Further broadening of the peak and a weak shoulder peak can be seen in Fig. 3(h) fitted with a blue curve due to the Fe−B bond, as detailed previously [34]. Under lithiation, a strong shoulder peak, fitted with a pink curve, at around 55.7 eV, as a

third component, can be observed in Fig. 3(i) that can be attributed to Li 1*s*, as pure Li 1*s* occurs at 55 eV. The blue curve corresponding to Li 1*s* is consistent with the Li 1*s* peak observed in Ref. [31].

D. Lithium ionics modulation of $Co_{40}Fe_{40}B_{20}$ magnetism

A typical stripe magnetic domain is observed over the $Co_{40}Fe_{40}B_{20}$ film by MFM, as shown in Fig. 4(a). This indicates the presence of a perpendicular magnetization component in thick $Co_{40}Fe_{40}B_{20}$ films. The magnetic hysteresis loops are measured under different $Co_{40}Fe_{40}B_{20}$ film states, in terms of charge (discharge) along the in-plane (out-of-plane) direction with respect to the $Co_{40}Fe_{40}B_{20}$ film plane, as shown in Fig. 4(b) [Fig. 4(c)]. In the out-of-plane direction, the saturation magnetization (M_s) after the first charge cycle increases from 900 to 1293 emu/cm^3, as shown in Fig. 4(d). Subsequently, with the 1st discharge, 100th charge, and 100th discharge cycles, the saturation magnetization values change to 926, 1295, and 930 emu/cm^3, respectively. The increase (decrease) in saturation magnetization can be better understood based on lithium forming (breaking) bonds with boron due to lithiation (delithiation). The conversion reaction of boron with $Co_{40}Fe_{40}B_{20}$ can happen by either addition or displacement reactions [27]. In the current case, B is the active element and Co and Fe are inactive elements towards the reaction with lithium ions. Thus, the lithium reaction with boron in $Co_{40}Fe_{40}B_{20}$ takes place via a displacement reaction. As a result, in the first charge cycle, the lithium bond with boron leads to it breaking its bond with Co and Fe. This results in a change of the boron position in close vicinity to Fe and Co that would lead to reconfigurations of the Fe-Co distances and affect exchange coupling due to a change in the orbital moment ratio [35]. In the pristine state, the magnetic moment of Fe-Co is lowered due to hybridization between B 2*p* states and 3*d* states of Fe-Co that leads to a reduction in the magnetic moment [34]. With lithiation. the magnetic moment of Fe-Co is increased as boron bonds with lithium and results in higher saturation magnetization. Furthermore, the uniaxial magnetic anisotropy (K_u) was calculated from magnetic hysteresis loops along in-plane and out-of-plane directions to understand the effect of lithiation on magnetic anisotropy and plotted versus the charge-discharge voltage, as shown in Fig. 4(d). In Fig. 4(c) lithiation results in a harder axis along the out-of-plane direction. As a result, K_u increases from the pristine state of 5.4×10^6 to 11.5×10^6 erg/cm^3 in the lithiated state [Fig. 4(d)]. In the amorphous $Co_{40}Fe_{40}B_{20}$ film, magnetocrystalline anisotropy is absent and anisotropy mainly depends on the orbital moment ratio. Anisotropy in $Co_{40}Fe_{40}B_{20}$ films can be stabilized by either bond-orientation anisotropy or pair-ordering anisotropy [36]. The former occurs when the density of bonds along in-plane and out-of-plane directions are different, resulting in the magnetic anisotropy. In the case of pair-ordering anisotropy, the difference in the like (Co, Fe) and unlike (Co or Fe and B) nearest neighbor distance occurs along in-plane and out-of-plane directions. In the present case, there is no source of bond-orientation anisotropy due to the absence of interfacial bond ordering, but pair-ordering anisotropy can occur under lithiation into

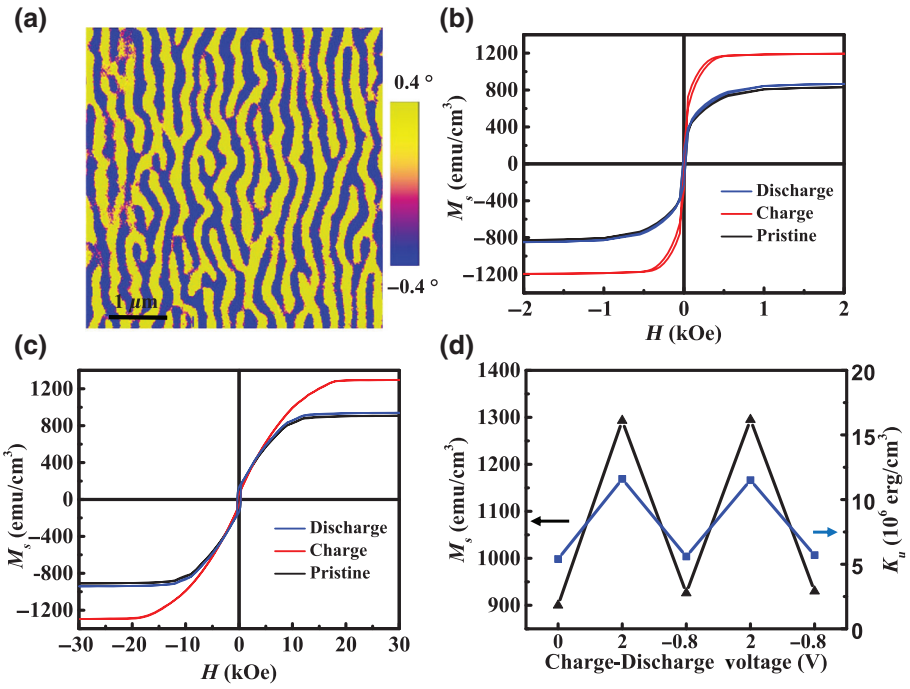

FIG. 4. (a) Typical MFM phase image over the $Co_{40}Fe_{40}B_{20}$ film surface exhibiting stripe domains. Magnetic hysteresis loop of $Co_{40}Fe_{40}B_{20}$ films from the pristine state to charged, and discharged (b) in-plane and (c) out-of-plane with respect to the $Co_{40}Fe_{40}B_{20}$ film. (d) Modulation of M_s and K_u under charge-discharge voltage.

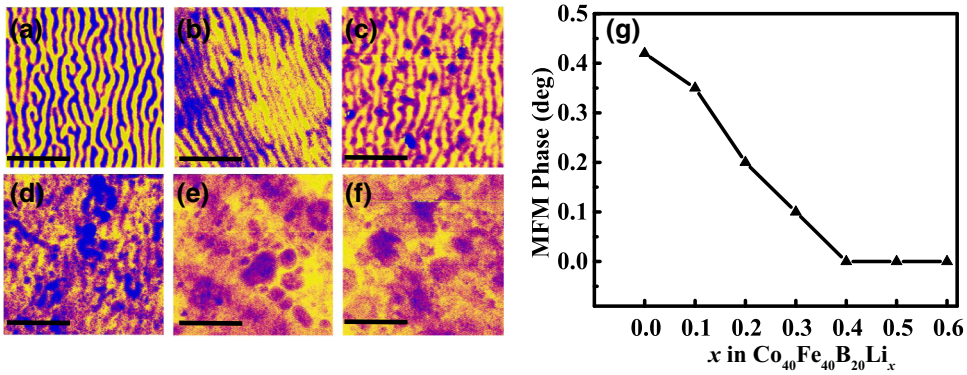

FIG. 5. MFM phase image for x in $Co_{40}Fe_{40}B_{20}Li_x$ equal to (a) 0.1, (b) 0.2, (c), 0.3, (d) 0.4, (e) 0.5, and (f) 0.6. The scale bars are equal to 2 μm. (g) Mean MFM phase values over stripe magnetic domains for different x values in $Co_{40}Fe_{40}B_{20}Li_x$.

$Co_{40}Fe_{40}B_{20}$ due to more interactions between like Co or Fe atoms, resulting in a change in the bond distance due to boron bonding with lithium. In addition, out-of-plane lithiation can push the Co-Fe atoms along the in-plane directions, resulting in more interactions of like Co-Fe atoms along the in-plane direction than those in the out-of-plane direction. Thus, pair-ordering anisotropy could result in a harder axis along the out-of-plane direction under lithiation. Also, the increased orbit moment ratio due to lithiation can stabilize anisotropy that leads to in-plane anisotropy [37].

To investigate the effect of lithiation on the magnetic domains, we perform *in situ* MFM after each galvanostatic charge. In the MFM measurements, the lift scan height of 100 nm is fixed for all measurements to allow a proper comparison. The quantification of the number of Li (x) per formula unit of $Co_{40}Fe_{40}B_{20}Li_x$ in the lithiated state can be determined by the Faraday laws of electrolysis under constant current electrolysis (Eq. 2), where M_{wt} is the molecular weight of $Co_{40}Fe_{40}B_{20}$, F is the Faraday constant, and C is the specific charge capacity:

$$x = \frac{CM_{wt}}{F}. \tag{2}$$

The $Co_{40}Fe_{40}B_{20}$ film lithiated to different x (lithium fraction) values from 0.1 to 0.6, and subsequently the MFM scan is performed to record the MFM phase image after each lithiation, as shown in Fig. 5. To understand qualitatively the effect of lithiation on magnetic domains, the mean phase value of the stripe magnetic domain contrast is calculated, which is proportional to sample magnetization [38,39]. This contrast is calculated by determining the phase value of the stripe domain of both upward and downward domain phase-contrast values over different stripe domain regions and taking the mean of both upward and downward phase contrasts to get the mean phase value. At a value of x equal to 0.1, the stripe domain shown in Fig. 5(a) is similar to that of the pristine state, as shown in Fig. 4(a), but the mean phase value decreases to 0.35° from 0.4° in the pristine state, as shown in Fig. 5(a). Upon further increasing the value of x to 0.2, the mean MFM phase decreases to 0.2, as shown in Fig. 5(b). When x is equal to 0.3, the mean phase value is 0.1°, as shown in Fig. 5(c). Further increasing the value of x to 0.4, 0.5, and 0.6, where no stripe domain is seen in Figs. 5(d)–5(f), leads to mean phase values approximated to zero. The effect of lithiation on magnetic domain structure is better seen in the plot of average MFM phase value versus different lithium concentrations in $Co_{40}Fe_{40}B_{20}$, as shown in Fig. 5(g). Thus, lithiation leads to a harder axis in the out-of-plane axis, as evidenced by a decrease in the MFM phase (sample magnetization) value with lithiation and the disappearance of the stripe domain at higher lithium concentrations.

IV. CONCLUSIONS

We utilize the all-solid-state Li^+ redox capacitor structure to modulate the magnetic properties of amorphous $Co_{40}Fe_{40}B_{20}$ thin films via a conversion reaction with lithium ions. The effect of lithiation-delithiation into $Co_{40}Fe_{40}B_{20}$ films on the magnetic anisotropy and magnetization are investigated. This study opens a way to control the magnetic properties of metallic magnetic thin films via an all-solid-state Li-ion redox capacitor. Also, the magnetism of crystalline magnetic electrodes, such as CoX (X = O, Sn, Sb, and Si), can be modulated via strain engineering that is induced and controlled by lithium ionics.

ACKNOWLEDGMENTS

This work is supported by the National Key R&D Program of China (Grant No. 2016YFA0201102), the National Natural Science Foundation of China (Grants No. 51871232, No. 51571208, No. 6171101158, No. 51525103, and No. 51931011), the Youth Innovation Promotion Association of the Chinese Academy of Sciences (Grant No. 2016270), the Key Research Program of the Chinese Academy of Sciences (Grant No. KJZD-EW-M05), the Ningbo Science and Technology Bureau (Grant No. 2018B10060), and the Ningbo Science and Technology Innovation Team (Grant No. 2015B11001).

[1] H. Wang, S. Xu, C. Tsai, Y. Li, C. Liu, J. Zhao, Y. Liu, H. Yuan, F. Abild-Pedersen, F. B. Prinz, J. K. Nørskov, and Y. Cui, Direct and continuous strain control of catalysts with tunable battery electrode materials, Science **354**, 1031 (2016).

[2] N. Lu *et al.*, Electric-field control of tri-state phase transformation with a selective dual-ion switch, Nature **546**, 124 (2017).

[3] A. Molinari, H. Hahn, and R. Kruk, Voltage-control of magnetism in all-solid-state and solid/liquid magnetoelectric composites, Adv. Mater. **31**, 1806662 (2019).

[4] B. Lei, N. Z. Wang, C. Shang, F. B. Meng, L. K. Ma, X. G. Luo, T. Wu, Z. Sun, Y. Wang, Z. Jiang, B. H. Mao, Z. Liu, Y. J. Yu, Y. B. Zhang, and X. H. Chen, Tuning phase transitions in FeSe thin flakes by field-effect transistor with solid ion conductor as the gate dielectric, Phys. Rev. B **95**, 020503 (2017).

[5] K. Terabe, T. Tsuchiya, R. Yang, and M. Aono, Nanoionic devices enabling a multitude of new features, Nanoscale **8**, 13873 (2016).

[6] B. Dieny and M. Chshiev, Perpendicular magnetic anisotropy at transition metal/oxide interfaces and applications, Rev. Mod. Phys. **89**, 025008 (2017).

[7] P. Dhanapal, S. Guo, B. Wang, H. Yang, S. Agarwal, Q. Zhan, and R.-W. Li, High-throughput investigation of orientations effect on nanoscale magnetization reversal in cobalt ferrite thin films induced by electric field, Appl. Phys. Lett. **111**, 162401 (2017).

[8] D. Chiba and T. Ono, Control of magnetism in Co by an electric field, J. Phys. D. Appl. Phys. **46**, 213001 (2013).

[9] T. Tsuchiya, K. Terabe, M. Ochi, T. Higuchi, M. Osada, Y. Yamashita, S. Ueda, and M. Aono, In situ tuning of magnetization and magnetoresistance in Fe_3O_4 thin film achieved with all-solid-state redox device, ACS Nano **10**, 1655 (2016).

[10] A. Molinari, P. M. Leufke, C. Reitz, S. Dasgupta, R. Witte, R. Kruk, and H. Hahn, Hybrid supercapacitors for reversible control of magnetism, Nat. Commun. **8**, 15339 (2017).

[11] A. Molinari, H. Hahn, and R. Kruk, Voltage-controlled on/off switching of ferromagnetism in manganite supercapacitors, Adv. Mater. **30**, 1703908 (2018).

[12] Q. Zhang, X. Luo, L. Wang, L. Zhang, B. Khalid, J. Gong, and H. Wu, Lithium-ion battery cycling for magnetism control, Nano Lett. **16**, 583 (2016).

[13] S. Dasgupta, B. Das, M. Knapp, R. A. Brand, H. Ehrenberg, R. Kruk, and H. Hahn, Intercalation-driven reversible control of magnetism in bulk ferromagnets, Adv. Mater. **26**, 4639 (2014).

[14] S. Dasgupta, B. Das, Q. Li, D. Wang, T. T. Baby, S. Indris, M. Knapp, H. Ehrenberg, K. Fink, R. Kruk, and H. Hahn, Toward on-and-off magnetism: Reversible electrochemistry to control magnetic phase transitions in spinel ferrites, Adv. Funct. Mater. **26**, 7507 (2016).

[15] C. Reitz, C. Suchomski, D. Wang, H. Hahn, and T. Brezesinski, In situ tuning of magnetization via topotactic lithium insertion in ordered mesoporous lithium ferrite thin films, J. Mater. Chem. C **4**, 8889 (2016).

[16] G. Wei, L. Wei, D. Wang, Y. Tian, Y. Chen, S. Yan, L. Mei, and J. Jiao, Reversible control of the magnetization of Fe_3O_4 via lithium ions, RSC Adv. **7**, 2644 (2017).

[17] G. Wei, L. Wei, D. Wang, Y. Chen, Y. Tian, S. Yan, L. Mei, and J. Jiao, Reversible control of magnetization of Fe_3O_4 by a solid-state film lithium battery, Appl. Phys. Lett. **110**, 062404 (2017).

[18] T. Tsuchiya, K. Terabe, R. Yang, and M. Aono, Interface nanoarchitechtonics for physical property tuning and enhancement, Jpn. J. Appl. Phys. **55**, 1102A4 (2016).

[19] Y. Zhang, X. Lin, J.-P. Adam, G. Agnus, W. Kang, W. Cai, J.-R. Coudevylle, N. Isac, J. Yang, H. Yang, K. Cao, H. Cui, D. Zhang, Y. Zhang, C. Zhao, W. Zhao, and D. Ravelosona, Heterogeneous memristive devices enabled by magnetic tunnel junction nanopillars surrounded by resistive silicon switches, Adv. Electron. Mater. **4**, 1700461 (2018).

[20] U. Bauer, L. Yao, A. J. Tan, P. Agrawal, S. Emori, H. L. Tuller, S. van Dijken, and G. S. D. Beach, Magneto-ionic control of interfacial magnetism, Nat. Mater. **14**, 174 (2015).

[21] L. Baldrati, A. J. Tan, M. Mann, R. Bertacco, and G. S. D. Beach, Magneto-ionic effect in CoFeB thin films with in-plane and perpendicular-to-plane magnetic anisotropy, Appl. Phys. Lett. **110**, 012404 (2017).

[22] C. Bi, Y. Liu, T. Newhouse-Illige, M. Xu, M. Rosales, J. W. Freeland, O. Mryasov, S. Zhang, S. G. E. te Velthuis, and W. G. Wang, Reversible Control of Co Magnetism by Voltage-Induced Oxidation, Phys. Rev. Lett. **113**, 267202 (2014).

[23] M. N. Obrovac and V. L. Chevrier, Alloy negative electrodes for Li-ion batteries. Chem. Rev. **114**, 11444 (2014).

[24] V. Aravindan, Y.-S. Lee, and S. Madhavi, Research progress on negative electrodes for practical Li-Ion batteries: Beyond carbonaceous anodes, Adv. Energy Mater. **5**, 1402225 (2015).

[25] N. Nitta and G. Yushin, High-capacity anode materials for lithium-ion batteries: Choice of elements and structures for active particles, Part. Part. Syst. Charact. **31**, 317 (2014).

[26] N. Mahmood, T. Tang, and Y. Hou, Nanostructured anode materials for lithium ion batteries: Progress, challenge and perspective, Adv. Energy Mater. **6**, 1600374 (2016).

[27] R. Benedek and M. M. Thackeray, Lithium reactions with intermetallic-compound electrodes, J. Power Sources **110**, 406 (2002).

[28] A. H. Whitehead and M. Schreiber, Current collectors for positive electrodes of lithium-based batteries, J. Electrochem. Soc. **152**, A2105 (2005).

[29] J. B. Bates, N. J. Dudney, B. J. Neudecker, F. X. Hart, H. P. Jun, and S. A. Hackney. Preferred orientation of polycrystalline $LiCoO_2$ films, J. Electrochem. Soc. **147**, 59 (2000).

[30] R. Manikandan, C. Justin Raj, M. Rajesh, B. C. Kim, S. Y. Park, B.-B. Cho, and K. H. Yu, Polycrystalline $V_2O_5/Na_{0.33}V_2O_5$ electrode material for Li^+ ion redox supercapacitor, Electrochim. Acta **230**, 492 (2017).

[31] X. Ding, X. Lu, Z. Fu, and H. Li, Temperature-dependent lithium storage behavior in tetragonal boron (B_{50}) thin film anode for Li-ion batteries, Electrochim. Acta **87**, 230 (2013).

[32] M. Schönleber, C. Uhlmann, P. Braun, A. Weber, and E. Ivers-Tiffée, A consistent derivation of the impedance of a lithium-ion battery electrode and its dependency on the state-of-charge, Electrochim. Acta **243**, 250 (2017).

[33] J. Li, X. Zhang, R. Peng, Y. Huang, L. Guo, and Y. Qi, $LiMn_2O_4$/graphene composites as cathodes with enhanced electrochemical performance for lithium-ion capacitors, RSC Adv. **6**, 54866 (2016).

[34] Y. Han, J. Han, H. J. Choi, H.-J. Shin, and J. Hong, Microscopic and electronic roles of B in CoFeB-based magnetic tunnel junctions, J. Mater. Chem. **21**, 14967 (2011).

[35] L. Reichel, L. Schultz, D. Pohl, S. Oswald, S. Fähler, M. Werwiński, A. Edström, E. K. Delczeg-Czirjak, and J. Rusz, From soft to hard magnetic Fe−Co−B by spontaneous strain: A combined first principles and thin film study, J. Phys. Condens. Matter. **27**, 476002 (2015).

[36] D. Kirk, A. Kohn, K. B. Borisenko, C. Lang, J. Schmalhorst, G. Reiss, and D. J. H. Cockayne, Structural study of amorphous CoFeB thin films exhibiting in-plane uniaxial magnetic anisotropy, Phys. Rev. B **79**, 014203 (2009).

[37] B. Cui, C. Song, Y. Y. Wang, W. S. Yan, F. Zeng, and F. Pan, Tuning of uniaxial magnetic anisotropy in amorphous CoFeB films, J. Phys. Condens. Matter. **25**, 106003 (2013).

[38] X. Zhu, J. Zhou, L. Chen, S. Guo, G. Liu, R.-W. Li, and W. D. Lu, In situ nanoscale electric field control of magnetism by nanoionics, Adv. Mater. **28**, 7658 (2016).

[39] P. Dhanapal, T. Zhang, B. Wang, H. Yang, H. Xuan, C. Bi, W. Wang, and R.-W. Li, Reversibly controlled magnetic domains of Co film via electric field driven oxygen migration at nanoscale, Appl. Phys. Lett. **114**, 232401 (2019).